The use of satellite products to assess spatial uncertainty and reduce life-time costs of offshore wind farms

Cleaner Environmental Systems 2 (2021) 100008

Contents lists available at ScienceDirect

Cleaner Environmental Systems

journal homepage: www.journals.elsevier.com/cleaner-environmental-systems

The use of satellite products to assess spatial uncertainty and reduce life-time costs of offshore wind farms

Simone Zen [a,*], Edward Hart [b], Encarni Medina-Lopez [a]

[a] Institute for Infrastructure and Environment, School of Engineering, The University of Edinburgh, UK
[b] Wind Energy and Control Centre, Department of Electronic and Electrical Engineering, The University of Strathclyde, Glasgow, UK

ARTICLE INFO

Keywords:
Satellite data
Wind speed
Significant wave height
Wind energy production
Spatial uncertainty
Offshore wind farm management

ABSTRACT

Managers of offshore wind farms make strategic decisions based on information about site wind speeds and significant wave heights (SWH) available from numerical weather predictions (NWP) or local in-situ measurements. However, the coarse resolution with which such information are available, both in space and time, introduces a high degree of uncertainty into the decision process which in turn may result in higher costs during different stages of offshore wind farm life. The current work investigates how space-borne data describing wind speeds and SWH might be used to quantify spatial uncertainties and support decisions during the design and operation of offshore wind sites. Results have revealed that due to high spatial variance of wind speed, the estimated wind power can differ from that provided by an offshore met mast up to 11%. The methodology proposed for SWH has shown how data collected from distinct satellites can be efficiently interpolated (maximum absolute error observed around 1 m) to generate high-resolute spatial information of sea water surface, regardless of satellite trajectory distributions. The work has provided insights on how the propagation of measurement uncertainty through the wind farm area can affect both management costs and wind energy production over the plant life-cycle.

1. Introduction

Decisions made during the life-cycle of an offshore wind farm are based on the data collected to characterize sea conditions. However, due to the remote areas where offshore wind farms are placed, data collection adds costs to a plant life-cycle during both the design and construction (e.g. foundation selection, fatigue estimates), and operational (e.g. asset maintenance) phases. This leads to the use of information with a coarse spatial resolution which is not ideal for describing spatial variations in sea conditions within the portion of sea covered by a wind farm, i.e. typically around 10 km^2. Uncertainty in sea conditions results in the application of large safety factors in the design of a wind farm (Hou et al., 2019), as well as a loss of available time windows to dispatch vessels during both the construction stage and operational stage (Browell et al., 2016; Lacal-Arántegui et al., 2018), increasing the cost of energy for offshore wind.

Information on wind speed and surface waves are commonly extracted from large numerical forecast models, or local measurements collected from instruments deployed for a specific time interval (e.g. buoy, LiDAR). A particularly relevant source for such data is provided by metocean services (Brownet al., 2018). Metocean (syllabic abbreviation of meteorology and oceanography) studies quantify weather and sea conditions (e.g. wind, waves, and water level). Metocean data combines in-situ measurements, numerical simulations, and satellite observations and supports the development and construction of offshore renewable projects, as well as their ongoing activity and maintenance. Although general data can be freely obtained within the public domain, offshore developments usually require site-specific measurements. This represents a cost that adds to the overall budget of an offshore renewable project. The need to combine three different measurement sources is given by the fact that in-situ measurements provide precise data for a spatially limited region. Numerical simulations, as well as data from satellite platforms, extend the spatial coverage of the information available from buoys, but suffer from limited spatial and temporal resolutions. Nevertheless, numerical models present the advantage of performing future projections after being properly calibrated with in-situ observations. The dataset provided by combining the aforementioned data sources is used to estimate statistics on the sea surface and weather conditions characterising a site.

Freely-available numerical models of the ocean area available from the ERA5 dataset collected for the public by the European Centre for Medium-Range Weather Forecasts (ECMWF) (ECMWF, 2020; Hersbach

* Corresponding author.
E-mail address: szen@ed.ac.uk (S. Zen).

https://doi.org/10.1016/j.cesys.2020.100008
Received 28 September 2020; Received in revised form 17 December 2020; Accepted 26 December 2020

et al., 2018). For sea state forecasting in the UK, the Atlantic – European North West Shelf operational model from Copernicus Marine Environmental Monitoring System (North West Shelf Seas, CMEMS-NWS) provides ocean wave analysis and forecast on a regular grid at 0.017° (Copernicus Marine Service, 2020a). Other data can be collected from marine buoy and radars located on the shore facing the offshore wind farm. In UK, the WaveNet database from the Centre for Environment, Fisheries and Aquaculture Science (CEFAS) collects real-time data on sea surface from a buoys network (CEFAS, 2020).

High-resolution data both in space and time is crucial to optimize the different stages of an offshore wind farm and reduce the associated costs. In particular, high temporal and spatial resolution wind speed values for large portions of sea would reduce the sources required for site choice, as well as driving the design of measurement campaigns, ultimately improving the accuracy with which energy production is estimated, thus the design of offshore plants, e.g. reduce safety factor values (Sempreviva et al., 2008). On the other hand, precise information on the significant wave height (SWH - measured in m), which is considered informative for the sea surface state, will reduce costs during both construction and operational phases, by improving the reliability in the forecast of windows for the dispatch of vessels (Lacal-Arántegui et al., 2018).

A precise knowledge of sea conditions appears crucial during offshore wind farms ongoing activities, since operation and maintenance costs can reach up to 30% of the total cost (Maples et al., 2013; Seyr and Muskulus, 2019). However, the coarse spatial resolution with which such measurements and numerical weather predictions (NWP) are available, i.e. 0.015–0.05° grid, makes it difficult to identify 3-h (roughly) windows for maintenance activities, leaving 4% of the time windows available for turbines maintenance unused (Browell et al., 2016). Because of such uncertainty in SWH measurements, probabilistic approaches are generally employed when identifying suitable time-windows for maintenance and optimization of operational and management costs (Carroll et al., 2016; Taylor and Jeon, 2018). Approaches apply distributions/models which describe the probability of turbine failures (this being what induces maintenance actions), these include Poisson processes, Weibull and Gamma distributions (see Seyr and Muskulus, 2019 for a complete review). Because of this, offshore wind farm projects deploy their own instrumentation in the area to characterize the wind field, e.g scanning LiDARs deployed on the coast facing the offshore wind farm area, or floating LiDARs. Advances in analysis of remote satellite data has revealed how the use of satellite platforms can provide high spatial resolution data to characterize the sea surface.

In this work, we focus on the important problem of characterising spatial variations/variability of wind speeds and wave heights across an offshore site, this being an important constituent factor within the wider context of information driven decision making outlined above. In particular, the aims of the work are: i) to use wind speed data retrieved from satellite synthetic-aperture radar (SAR) imagery to assess uncertainty in estimating wind power compared to standard measurement techniques (i.e. the standard measurement technique provides a single value over the wind farm area); ii) to propose a new methodology that allows the generation of surface maps from along-track SWH measurements extracted from satellite altimeters.

The paper is structured as follows. Section 2 presents a brief description of the satellite products used for the analysis. Section 3 presents the methodology for both wind power computed from wind field retrieved from SAR imagery, and SWH 2D maps generated from along-track information from satellite altimeters. Results are presented in Section 3. In section 4 the methodology proposed and its relevance for offshore wind farms management is discussed. Finally, Section 5 summarize the work and main findings.

2. Satellite products to characterize sea surface

SAR sensors have been found able to provide information on wind spatial variability at high spatial resolution, even close to coastal areas (Zecchetto, 2018). Such sensor measures variations on a surface by sending an electromagnetic impulse and recording the returning signal. Both the emitted and recorded signals can be polarized by adjusting the electric field with a polarization perpendicular to the direction of wave propagation. The polarization can be horizontal(H) or vertical (V) and SAR sensors are catalogued according to the polarization of receiving and transmitting signals, i.e. VV, HH, VH, or HV (they can both be vertical or horizontal, or one vertical and the other horizontal). After bouncing on the surface, the emitted signal is scattered back to the sensor and its strength is analysed using different polarizations to gain information about the observed object/surface. In SAR imagery three surface scattering mechanisms are considered, namely rough surface, volume, and double bounce. Rough surface, e.g. bare ground and water surface, presents a strong scattering in VV polarization, therefore SAR sensors used to examine sea surface adopt a VV polarization (Flores-Anderson et al., 2019).

Sentinel-1A launched in April 2014, and it was the first satellite mission of the European Space Agency (ESA) provided with a SAR imaging sensor. Two years later, the Sentinel 1-B mission was added to its orbit to increase temporal coverage of maritime and land monitoring (European Space Agency (ESA), 2020). In case of flat surfaces the incident angle of the signal is equal to that of the reflected one which is not recorded by the sensor. On the other hand, in rough surfaces the signal bounce back in all the directions and part of the returning signals reach back the sensor antenna with strength and delay proportional to local surface changes (Ulaby et al., 1982). In sea environment, the backscatter of the signal generates the image which features represent the sea surface signature associated to wind field conditions. Therefore, SAR images collected from a satellite contain indirect information on wind speed and direction. Based on this, different methods have been developed to retrieve wind speed information from SAR imagery and generate high-resolution maps for the wind field observed over the sea. Geophysical models calibrated using wind directions extracted from global numerical models, radar frequency, polarization, and incident angle (e.g. Monaldo et al., 2016; Ahsbahs et al., 2017; Rana et al., 2019) and Two-Dimensional Continuous Wavelet Transforms (e.g. Zecchetto, 2018) have been used to retrieve wind speed information from SAR satellite imagery. The latter presents the advantage respect to geophysical methods of not requiring external inputs to calibrate the parameters.

Further information on sea surface height, and in particular, significant wave height (SWH), have become globally available since the launch of satellite missions provided with altimeters. Missions include Cryosat-2 (since 2010), SARAL/AltiKa (since 2013), Jason-2 (since 2008), Jason-3 (since 2016), Sentinel-3A (since 2016) and Sentinel-3B (since 2018). The altimeter transmits microwave pulses toward the Earth and records the signal reflected back. The time gap between the emitted and received signal indicates the distance of the surface from the satellite. Because the position of the satellite is known, thanks to a GPS system, this is translated in surface height with respect to the referenced ellipsoid (approximation of Earth's surface). From the measurements collected of sea surface, SWH is defined as the mean of the highest one-third of all waves observed as

$$SWH = \frac{1}{N/3}\sum_{i=1}^{*} H_i, \tag{1}$$

where H is the wave height, i is the number of high waves (assuming waves are ordered from highest wave height to lowest wave height), and N is the total number of waves observed over a specific time period (Holthuijsen, 2010). Data on SWH recorded from satellite altimeters are considered a reliable source since they have been validated against buoys and cross-validated with other satellite altimeters (Yang and Zhang, 2019). The Copernicus Marine service provides a globally distributed dataset for SWH that combines along-track measurements from the following satellites: Jason-3, Sentinel-3A, Sentinel-3B, Cryosat-2 and SARAL/AltiKa. Data from each mission are homogenized based on the

Jason-3 mission and validated against marine buoys. The service generates near-real time products, collecting available along-track measurements, with each file covering a 3-h time window (Copernicus Marine Service, 2020b).

3. Method

3.1. Wind field

Wind speed maps produced by the Wind Energy Department of the Technical University of Denmark (DTU) (DTU Wind Energy, 2020) have been used to characterize changes in wind speed and, consequently, wind power within the study area. The wind field products provide wind speed at 10 m above the sea surface as retrieved from SAR data provided by the European Space Agency (ESA). For this analysis, we used the wind field retrieved from the C-band SAR imagery of Sentinel 1 missions A and B for the period January to March 2020. These maps have been produced with a resolution of 0.009° x 0.006° (longitutide x latitude), and with the same time resolution of Sentinel 1A and B. However, several satellite passages can cover the study area increasing the frequency with which such wind products are available. For the analysis a total of 31 SAR-derived products were collected. An example of the second level product available from DTU Wind Energy is shown in Fig. 1. The area of interest, covering the portion of sea of the wind farm, was extracted from the complete map provided by DTU in order to obtain a detailed map of the wind field within the wind farm. This product was then used to quantify the error generated when assuming constant wind speed within the study area. Furthermore, we estimated how such error in the measurements propagates into the wind power in different areas of the wind farm.

The wind power, P_W, was computed as (Leithead, 2007)

$$P_W = \frac{1}{2}\rho C_p A_r U^3, \tag{2}$$

ρ is air density, A_r is the area swept by the rotor, and U is the wind velocity at hub height. The wind power is converted into the actual power extracted from the turbine rotor by using the power coefficient C_p which accounts for turbine design. The value ranges between 0 and 0.5 (Leithead, 2007) and for this work was set equals to 0.4 to remain conservative. Since the current aim is to explore variability across a wind farm, the specific value of C_p will not impact overall findings. In practical applications efficiency values would be supplied by the wind turbine manufacturer.

Because wind speed data extracted from SAR imagery referred to the wind speed observed 10 m above the sea surface, a preliminary operation was needed to convert such value to wind speed at the hub height. This can be done by recalling the well known logarithmic profile characterising wind within the atmospheric boundary layer. Under the hypothesis of stable atmospheric conditions the logarithmic law for the vertical profile of wind velocity $U(z)$ reads (Tennekes, 1973)

$$\frac{U(z)}{u_*} = \frac{1}{\kappa} log\left(1 + \frac{z}{z_0}\right), \tag{3}$$

where z is the height above the ground, u_* is the friction velocity, κ is the von Karman constant equals to 0.41, and z_0 is the surface roughness length. In a turbulent regime, this latter quantity depends on the flow field rather than the geometrical roughness of a surface (in this case sea waves). (Charnock, 1955) proposed that for air above water surface the non-dimensional relationship between the roughness length and the friction velocity was constant and equals to 0.0144. Such relationship allows the roughness length, z_o to be estimated according to

$$z_0 = \alpha \frac{u_*^2}{g}, \tag{4}$$

where $\alpha = 0.0144$ is the Charnock's constant (Charnock, 1955) and g is the acceleration due to gravity. By substituting equation (4) into equation (3) we obtain an implicit function of u_* that can be solved once the height z and the related velocity $U(z)$ are known. Therefore, wind speed observed at a specific height can be used to estimate the friction velocity, which is the unknown of the obtained implicit function, and describes the turbulent flow field (Schneiderhan et al., 2005; Badger et al., 2010). Badger et al. (2010) adopted such technique, along with measurements of wind speed collected up to 90 m to extract the wind speed at 10 m above the sea surface and asses wind speed retrieved from SAR. In this work, wind speed from wind SAR-derived maps is used to compute first the friction velocity and then, trough equation (3) the wind speed at the hub height, which for the wind turbines of Beatrice wind farm (case study) is equals to 101 m.

The newly generated wind field obtained from the satellite second level product, i.e. wind speed at hub height, was fed into equation (2) to generate wind power maps. Such values were then compared with the value of wind power estimated by assuming a constant wind velocity, equals to wind field average, in the whole study area. Results were used

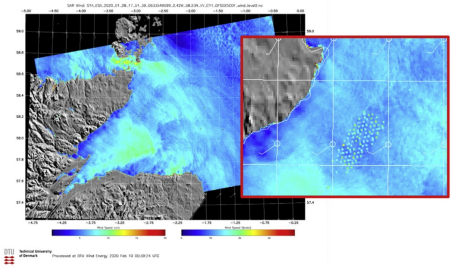

Fig. 1. Example of wind field map generated from DTU Wind Energy (2020). The image shows the wind speed 10 m above the sea surface as retrieved from the SAR data collected from Sentinel 1A on the 28 of January 2020 at 5:52 p.m. Scotland's outline is shown for geographical reference. Image closeup highlights the turbines constituting the offshore wind farm Beatrice (Beatrice Offshore Wind Fa, 2020). This is only an example of the satellite-derived product used in the analysis, which high resolution version can be found at DTU Wind Energy (2020).

to quantify the error in using one value of wind speed during both design and operational phases in a offshore wind farm lifetime.

3.2. Significant wave height

Data on significant wave height were collected from third level (L3) satellite product available at the Copernicus Marine Service (Copernicus Marine Service, 2020b). The service provides global ocean significant wave height by processing near-real-time data from along-track altimeter of several satellite missions including Jason-3, Sentinel-3A, Sentinel-3B, Cryosat-2 and SARAL/AltiKa. Files are generated for a three-hour time window and present one point every 7 km along the satellite trajectory. The same service produces also fourth level (L4) products by merging together all Significant Wave Height measurements available from the level 3 product. The data is organised in 2° mesh covering the global ocean. However, the coarse resolution of this latter L4 product did not allow us to use it to describe changes in sea surface within a small area such as that typically covered by an offshore wind farm. Therefore, the SWH measurements available from the L3 product were interpolated to generate a map of SWH for the area covered by the offshore wind farm. The small portion of sea covered by the area of interested limited the amount of trajectories available for the interpolation. For this reason, the interpolation procedure focused on a more extensive area (in order to include as many trajectories from different satellites as possible) to then obtain the SWH values in the study area.

Because the methodology and the resolution of the grid chosen for the interpolation could affect the quality of the results, different methodologies and grid resolutions were explored. In particular, three types of interpolating methods were tested covering an increasing range of complexity, including linear, nearest and cubic method. The linear and cubic method respectively use a first and third degree polynomial to interpolate data within the domain. The nearest method expands the information from the cells carrying the data to their neighbours. The analysis was performed using the data from the satellites passing through the study area within a 24h window. The interpolated values obtained by using different interpolating methods, and space and time resolutions were then validated by using in-situ measurements recorded from a marine buoy (see section 4.1).

4. Validation against in-situ measurements

4.1. Case study

The location of the offshore wind farm Beatrice was chosen for the analysis. The Beatrice wind farm is Scotland's largest operational wind farm, it is located in the North Sea, approximately 13 km from the Caithness shore, North-East Scotland, precisely in the Moray Firth (see Fig. 3). This site contains 84 S-Gamesa turbines, with hub heights of 101 m and rotor radii of 77 m, which provides a total installed power capacity of 588 MW, and covers an area of 131.4 km^2 (Beatrice Offshore Wind Fa, 2020). The wind farm is fully operational since June 2019. The analysis of wind speed and SWH was conducted on the minimum portion of sea containing the offshore wind farm, which is represented in Fig. 3 with a yellow polygon labelled with the number "2". The dashed line describes the geographical limits of the wind farm. To allow a larger number of satellite trajectories in the computation of the SWH, the study area was extended to a larger portion of sea which extends from 57° to 60° latitude, and from -5° to 0° longitude (see the blue box in Fig. 3).

4.2. Marine buoy

In-situ SWH measured at a buoy located in the Moray Firth at 57°57'.99N, 3°19'.99W, was used to validate the satellite-derived SWH (see Fig. 3). The buoy is within the extended area used for the interpolation and belongs to the network of buoys distributed along the UK coastline and managed by the Centre for Environment Fisheries and Aquaculture Science (Cefas) (WaveNet, 2020). Data on SWH, peak direction, and sea temperature are collected from each buoy within the network with a 30-min resolution.

First, the values extracted from the altimeter were directly compared with those measured at the buoy at the same time (i.e. within a 15 min interval). The difference between the SWH extracted from the altimeter, SWH_{alt}, and the SWH measured at the buoy, SWH_{buoy}, was computed for all the points along the track of the satellites passing through the study area within the specified time window. The value of such a difference was then related to the distance between the location where the altimeter collected the measurement and the position of the buoy. Hereinafter we will refer to this difference as altimeter-buoy difference. Second, the interpolated value extracted at the buoy position, SWH_{int}, was compared with that measured at the buoy and related to the minimum distance observed during the 24h window between satellite trajectories and buoy position. Because the interpolating procedure used all the data available for the area in one day, the interpolated value extracted at the buoy position was compared with the average, 25th percentile, and 75th percentile of the measurements collected daily from the buoy. Hereinafter, such difference will be denoted as interpolate-buoy difference and indicated, respectively, with the symbol Δ_{mean}, Δ_{25}, Δ_{75}. Finally, the interpolate-buoy difference was related to the percentage of area covered by the smallest polygon containing all the trajectories observed during the time window.

Fig. 4 shows the data of SWH collected from the buoy for the time period that goes from 1 January 2020 to 30 March 2020. The measurements are organised in measurement distribution per day. Boxes show measurements comprised between the 25th and 75th percentile, bars show the remaining part of the distribution, circles represent the distribution outliers, and the orange continuous line links the daily average of the SWH measurements.

Table 1 summarizes the main characteristics of the different sources used for the analysis. From, the table it is possible to notice that the length of the time window explored in the work was determined by the availability of the data from satellite altimeters which dataset dates back to the 01 January 2020.

5. Results

5.1. Wind field and wind power

The wind field retrieved from Sentinel-1 SAR imagery was used to estimate the error in power estimate when the wind is assumed to blow at a constant speed in the whole area covered by the offshore wind farm (equivalent to the single measurement in the farm provided by a classical meteorological mast). An example of the results obtained are reported in Fig. 6. The four panels of Fig. 6 are organised in a matrix where the columns are 'Value' and 'Error', and the rows are the variables, i.e. 'wind speed' and 'wind power'. The average wind speed at hub height, i.e. 9.94 m/s, computed from the wind field of Fig. 6a was used to estimate the error in assuming constant the wind velocity when NWP are extended to the whole wind farm (Fig. 6b).

The wind field in Fig. 6a is then used to feed Equation (2) and estimate changes in wind power and, thus, potential energy production (Fig. 6). The wind power generated by the average wind speed is called inferred wind power and it is reported on top of panel c. For the case study the inferred wind power generated by a wind blowing at 9.94 m/s equals to 4.5 MW. The difference between this value and those associated to the complete wind field (Fig. 6c) is reported in Fig. 6d as a percentage. Because wind power is proportional to wind speed cubed (see equation (2)), the error in power (Fig. 6d) is three to five times higher than that for wind speed itself.

Changes in wind speed from 10 m above the sea surface to the hub height were observed not to modify the spatial pattern of the wind flow field, but its magnitude. The difference between the average minimum, and maximum values for the study area for the two distributions (i.e. 10-

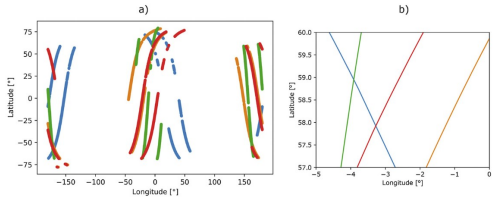

Fig. 2. Along-track SWH measurements for the trajectories crossing box 1 in Fig. 3 during the 01 January 2020; a) the whole trajectories and b) the trajectories within the study area (box 1 Fig. 3). In this example the satellites include Sentinel-3B, Cryosat-2 and SARAL/AltiKa both ascending and descending trajectories.

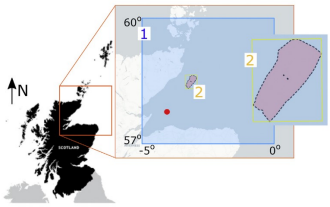

Fig. 3. Scotland's map showing the geographical position of the offshore wind farm Beatrice (pink polygon with dashed contour). The blue (label 1) and yellow (label 2) boxes indicate, respectively, the extended area used for the SWH analysis and the minimum polygon containing the portion of sea covered by the wind farm. The red dot indicates the marine buoy used to validate the results. Figure closeup provides details on the wind farm geometry.

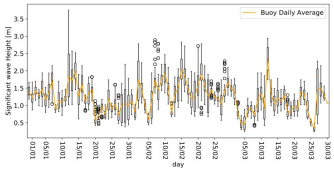

Fig. 4. Daily distribution of the SWH measured at the buoy located in the Moray Firth. The measurements are organised daily and the box represent the data comprised between the 25th and 75th percentile of the entire measurement distribution for a day. Bars are the remaining part of the distribution and circles the outliers. The orange continuous line links the average value observed each day. Data are freely available from WaveNet (2020).

meter and hub-height wind speed) was observed to be, respectively, 2.085 m/s, and 2.63 m/s; with an overall average difference around 2.45 m/s. Also, the standard deviation computed for the two distributions showed very little differences with an average value around 0.53 m/s and 0.42 m/s for the hub-height and 10-m wind speed

Table 1
Distinct Sources used in the analysis and related characteristics. In the columns title Res means resolution. * The time resolution is that of Sentinel1A and B, therefore the same imagery is available every 12 days. However, several satellite passages can still cover the study area increasing the product frequency.

Source	Space Res [lat; long]	Time Res	Interval [since]
SAR-derived maps	0.009°; 0.006°	*	2002
Satellite altimeter	7 km (along-track)	several times per day	01/01/2020
Marine buoy	–	30 min	08/12/2019

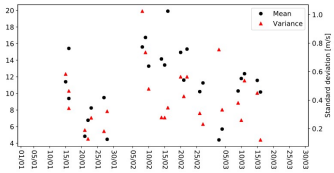

Fig. 5. Panels show the mean (black dot) and standard deviation (red triangle) for the wind field observed within the study area in the months of January, February, and March 2020.

distribution, respectively. These values show that, on average, the hub-height speed distribution is the 10-m speed distribution which values are shifted of a small amount, i.e. 2.4 m/s for the case study.

Finally, the 2D maps describing wind field can be described by the statistics of the distribution of their values. By using the first two moments, mean and standard deviation, of wind speed values collected in a specific date, we can provide a synthetic description for the entire dataset. Fig. 5 shows the mean (square) and standard deviation (triangle) for the wind speed observed 10 m above the sea surface. These statistics can be used to describe the condition of the sea by associating an increase in wind speed standard deviation to spatial changes in sea level. In addition, since wind power is directly related to wind speed, such statistics provide also information on the behaviour of wind power mean and spatial variance.

5.2. *Small scale variations in SWH*

Fig. 7a) shows the distribution of the altimeter-buoy difference values observed in each date for the three months analysed. Boxes include

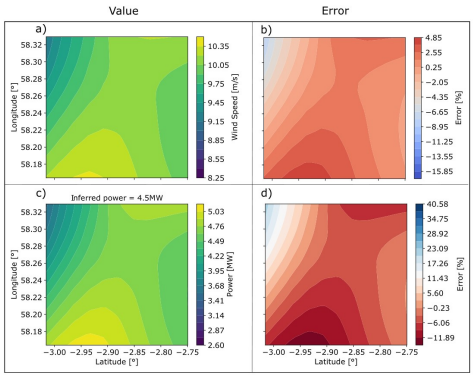

Fig. 6. Wind speed at hub height within the study area obtained from the wind field retrieved from Sentinel-1A SAR image (panel a). Panel c) shows the energy power associated to the flow field in panel a). The inferred power is the energy power computed by using the average wind speed value observed from the wind field at hub height. The Error column (panels b and d) presents the error when the velocity speed is assumed constant within the area, both for the b) wind speed and d) energy power. The error was estimated assuming the constant value equal to the average speed observed within the study area.

values within the 25th and 75th percentile, the bars are the remaining values, and the circles represent the distribution of outliers. Most of the observed dates have quite stretched distributions covering a measuring gap between 3 and 5 m. There are also few dates presenting a narrow distribution (e.g. the values between the 25th and 75th percentile show a difference around 1m), such as 22 January; 2, 12, 14, 28 February; and 15, 20, 25 March. Additional information on the reliability of the measurements from the altimeter can be obtained by relating the values of Fig. 7a) to the distance between the point of the sea surface were the measurement was taken, and the position of the buoy. Results are presented in Fig. 7b). The scatter plots present the altimeter-buoy difference extracted along the track for each satellite and are grouped in dates. From Fig. 7b) we can observe that there is not a clear relationship between distribution variance and average distance of the satellite from the buoy. Indeed, for the aforementioned dates characterised by a small variance, the measurements spread between 0 km and 200 km from the buoy. Although the graphs show an overall trend where the gap between the two measurements becomes bigger the further we move from the buoy, it is not possible to establish a clear relationship between measurement precision and distance from the buoy. Nevertheless, within a 50 km range distance, almost all the measurements (only one pass during the 22nd of March 2020 shows an increasing trend) show satellite measurements close to the in-situ one, with differences between them ranging from −0.3 m to 0.5 m.

To extend the observation from the satellite to a wider area, along-track measurements from the altimeter were interpolated over the domain represented by polygon "1" in Fig. 3, and data were organised in a regular mesh grid. An example of the interpolation results is reported in Fig. 8 for the three different interpolating methods, using the along-track data of the satellites passing through the study area on the 01 January 2020, which trajectories are reported in Fig. 2. The three panels of Fig. 8 are represented from left to right, with increasing complexity in the method used for data interpolation. By considering the same mesh resolution for the three methods, the cubic interpolation of the altimeter measurements provided the most detailed map for SWH. Nevertheless, the comparison of the interpolated value extracted at the buoy location and the SWH values measured at the buoy identified the nearest method as the best interpolating method for our purpose. Fig. 9 reports the results of this analysis conducted for all the 28 dates for which measurements from the altimeter were available within the three months observed (different colours in Fig. 9). For the nearest method, 7 of the dates analysed are aligned along the agreement line (continuous line), 13 dates are within the 30% interval (dashed lines), and in 8 dates the measurements from the altimeter overestimated those from the buoy of more than 30%. Therefore, for the 71.4% of the dates observed the value recorded from the altimeter differed from the measurements collected in the whole day at the buoy, i.e. values comprise between the 25th and 75*th* percentile of the measurement distribution (horizontal lines in Fig. 9), of a quantity less or equal to 30%. On the other hand, for the linear method, only in two dates the interpolated values are close to the agreement line, and for 8 dates they are within the 30% interval. For this method, in the majority of the dates analysed, i.e. 18 dates (64%), the interpolation overestimated the measured value at the buoy by more than 30%. Finally, even worse results were obtained by interpolating the measurements from the altimeter with a cubic relationship. In this case, 2 dates lay on the agreement line, 7 are included within the 30% interval of confidence, and for the remaining dates, i.e. 19 (69%), the satellite altimeter overestimated the SWH by more than 30% of its value.

Because results from the interpolation procedure can be affected by the size of the mesh used, different grid resolutions with decreasing mesh size were explored. The sensitivity analysis revealed no changes in interpolation results when the ratio between number of cells along the y (latitude) and x (longitude) direction is kept to 1. Nevertheless, increasing this ratio showed good results, providing interpolation values close to those observed at the buoy. The analysis was performed for the three different methods for a set of cell ratios ranging from 0.5 to 2.5, and the mean error estimated as the mean of the interpolation-buoy difference observed during the three months was computed. Fig. 10a shows the result of the sensitivity analysis conducted. The three curves collecting the mean error of the interpolate-buoy difference for each of the cell ratios explored present an upward opening with a minimum error value reached when the cell ratio is equal to 1.5, 1.7, and 1.8, respectively for

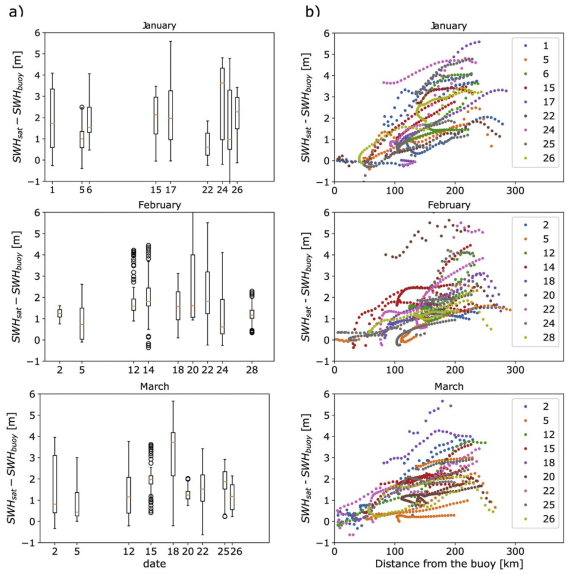

Fig. 7. Panels show a) the distribution of the difference between SWH values measured from the altimeter and those measured from the buoy observed during a 24-h window. b) The same values from a) are organized according to the distance between the point measured by the altimeter and the buoy position. Boxes in a) indicate the portion of the distribution comprises between the 25th and 75th percentile, bars the remaining part of the distribution, and circles are the outliers. Plots show the data available for the months of January, February, and March 2020.

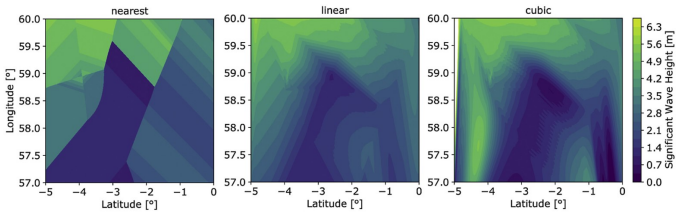

Fig. 8. Results of the interpolation of the along track measurements by using three different interpolating methods: linear, nearest, and cubic. Plots are obtained by using the data recorded on the 01 January 2020 by the altimeter of different satellites which trajectories are presented in Fig. 2.

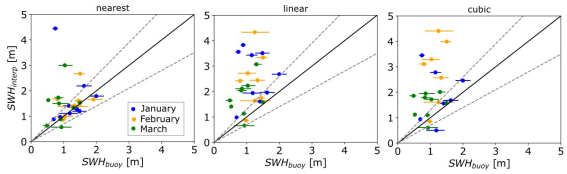

Fig. 9. Comparison between the interpolated value extracted at the buoy position and the average value of the measurements collected at the buoy on the same date for the three months. The horizontal line indicates the data comprises between the 25th and 75th percentile of the daily distribution of the measurements collected from the buoy. Results are reported for the three interpolating methods used, namely linear, nearest, and cubic.

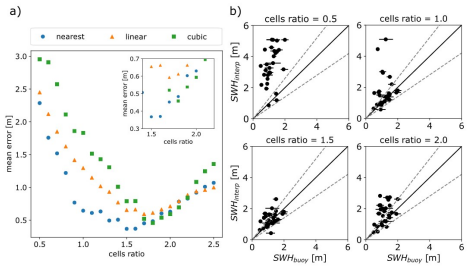

Fig. 10. Mean interpolate-buoy difference observed in the study period of three months. a) The error plotted against the ratio between the number of cells used along latitude and longitude for the interpolation, for the three different methods used: nearest (blue circle), linear (yellow triangle), and cubic (green square). b) Results from the nearest method. Comparison between the interpolated value extracted at the buoy position and the average value of the measurements collected at the buoy on the same date for the three months for some values of the cells ratio. The horizontal line indicates the data comprises between the 25th and 75th percentile of the daily distribution of the measurements collected from the buoy.

nearest, linear, and cubic method. However, the more precise method resulted to be the nearest one, with a minimum mean error of 0.37 m. Panels of Fig. 10b show how the comparison between the interpolated values, SWH_{interp} and those measured at the buoy, SWH_{buoy}, changes by varying the cell ratio for the latter method, i.e. the nearest. Interestingly, within the range 1.8–2.0, the cubic method presented errors lower than those obtained by adopting the nearest one, with a minimum mean error of 0.46 m (see Fig. 10a). Hereinafter, the analysis will be carried out by using the nearest method with a grid presenting 750 and 500 cells, respectively, in the vertical and longitudinal direction (latitude, longitude); thus a cells ratio equals to 1.5. Under such conditions, the generated map for SWH shows a resolution of 0.004° lat and 0.01° long.

Fig. 9 shows that in some dates the interpolation performs better than others. To explore the reason behind this we observed the minimum distance between the satellite trajectories and the buoy, as well as the portion of study area covered by all the trajectories. A graphical representation is reported in Fig. 11 for all the dates collected. The continuous lines and shadowed areas represent, respectively, the satellite trajectories and the portion of study area covered. Fig. 12 reports the interpolate-buoy difference against the minimum distance from satellite altimeter and buoy observed during the day (Fig. 12a), and the spatial coverage of the trajectories (Fig. 12b). Particularly, the interpolate-buoy difference was computed as difference between the interpolated value extracted at the buoy position and the mean, 25th percentile, and 75th percentile value of the daily distribution of the measurements collected at the buoy, and respectively indicated as Δ_{mean}, Δ_{25}, and Δ_{75}. From the latter plot, it seems clear that the quality of the interpolation cannot be associated to the proximity of the measurements used for the interpolation to the buoy, nor to the distribution, i.e. spatial coverage of the satellite trajectories.

Data reported in Figs. 11 and 12 are summarized in Table 2. The table includes information on the interpolate-buoy difference (i.e. Δ_{mean}, Δ_{25}, and Δ_{75}), the minimum distance observed from the buoy, and the spatial coverage of the study area from the satellite trajectories.

To better understand why for some dates the interpolating procedure performed better than others, the profile for the SWH extracted from each satellite was compared with that observed during the same 24-h window from the buoy. The analysis was performed for three dates, the 1st, 6th, and 22nd of January 2020. Results are reported in Fig. 13. These dates were chosen since they showed, respectively, low values for minimum distance from the buoy and high values for Δ_{SWH}, high values for minimum distance from the buoy and high values for Δ_{SWH}, low values for minimum distance from the buoy and low values for Δ_{SWH}, as it is shown in Fig. 13a. In Fig. 13a, labels indicate the date, while circles and vertical lines represent, respectively, the interpolate-buoy difference obtained by using the mean daily value recorded at the buoy, the 25th and 75th percentile of the daily distribution of the measurements at the buoy. The SWH profiles recorded at the buoy (dashed black line) and the along-track values used for the interpolation (continuous coloured line) are reported for the different dates in the panels b, c, and d of Fig. 13. Here the close ups present the spatial distribution of satellite trajectories and buoy.

The profiles recorded from the altimeters during the 1st of January 2020 (Fig. 13b) show a SWH ranging from 0.98 m to 5.39 m. Moreover,

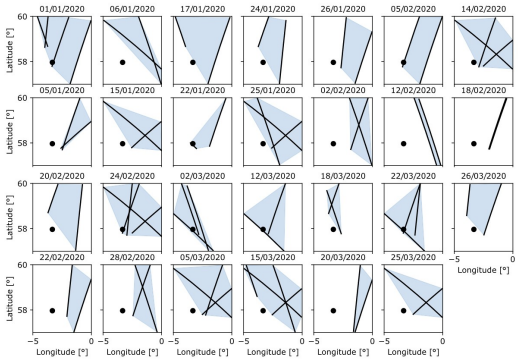

Fig. 11. Satellite trajectories (continuous line) and their spatial coverage (light blue polygon) for each date analysed. Black circles represent the position of the buoy.

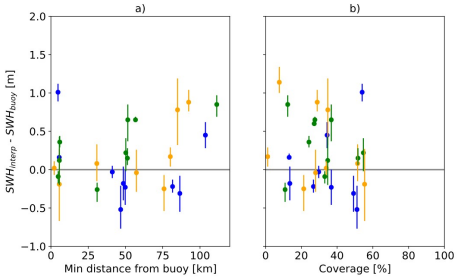

Fig. 12. The interpolated-buoy difference is plot against a) the minimum distance of the measurements extracted from the satellite altimeter from the buoy, and b) the distribution of the trajectories as portion of the study area included within all the trajectories. The plot present the interpolate-buoy difference computed as the interpolated value extracted at the buoy and the mean (circle), the 25th percentile (vertical line lower extreme), and the 75th percentile (vertical line upper extreme) of the daily distribution of the measurements collected at the buoy. The horizontal grey line indicates the perfect match between the two sources. Colours refer to different months, with blue, yellow, and green being associated to January, February, and March, respectively.

the information on the SWH extracted from the altimeter combined with the spatial distribution of the trajectories reported in the closeup of Fig. 13b revealed significant spatial changes in SWH. Trajectories 1,2,3, and 4 are respectively SARAL/AltiKa (ascending), SARAL/AltiKa (descending), Cryosat-2 (descending), and Sentinel-3B (descending). Therefore, the upper part of the study area, i.e. first measurements in the profiles 3 and 4, and last measurements in the profile 1, presents high values of SWH around 5.5 m, while the lower part of the study area is characterised by SHW values between 0.98 m and 3.58 m. As a results the interpolation provides a value of SWH which is 1 m higher than the average values of 1.41 m measured at the buoy during the day (25th percentile = 1.3 m, 75th percentile = 1.53 m). Analogously, in day 6^{th} of January 2020 the SWH recorded from the altimeters showed high variability with values ranging from 2.7 m to 4.92 m (see Fig. 13c). As trajectories 1 and 2 in the closeup represent respectively Jason-3 (descending) and Sentinel-3A (ascending), also in this date the upper part of the study area was characterized by higher SWH compare to the lower part. Nevertheless, when comparing with the profiles of Fig. 13b (profiles 1 and 2), they show a similar behaviour, with profile 1 reaching smaller values in the second part. The reduced spatial variability in SWH within the study area may be the explanation to the difference of 0.45 m between the interpolated value and the average SWH value of 1.15m recorded at the buoy for the day (25th percentile = 0.98 m, 75th percentile = 1.33 m). Finally, we explore the values recorded by the altimeters for the date 22 January 2020 that presented a difference of 0.16 m between the interpolated value and the average SWH of 0.69

Table 2
Interpolate-buoy difference, Δ, minimum distance observed from the buoy, d_{min}, spatial coverage of the study area from the satellite trajectories, Coverage, and number of measurements used for the interpolation. The interpolate-buoy difference was computed as difference between the interpolated value extracted at the buoy position and the mean, 25th percentile, and 75th percentile value of the daily distribution of the measurements collected at the buoy. Respectively, indicated as Δ_{mean}, Δ_{25}, and Δ_{75}.

Date	Δ_{25}	Δ_{75}	Δ_{mean}	d_{min}	Coverage	Measurements
	[m]	[m]	[m]	[km]	[%]	[number]
01/01/2020	−0.09	−0.32	−0.20	4.72	54.02	128
05/01/2020	−0.08	−0.51	−0.30	48.54	13.58	76
06/01/2020	0.59	0.24	0.42	103.63	34.42	107
15/01/2020	0.02	−0.44	−0.20	49.83	36.75	89
17/01/2020	−0.09	−0.56	−0.32	86.48	49.21	71
22/01/2020	0.07	0.03	0.03	5.53	13.21	46
24/01/2020	0.75	0.58	0.66	81.60	26.78	67
25/01/2020	−0.45	−1.02	−0.76	46.80	51.14	127
26/01/2020	0.05	−0.11	−0.03	41.17	29.73	80
02/02/2020	1.04	0.76	0.88	92.41	28.90	90
05/02/2020	−0.05	−0.24	−0.15	2.19	33.95	73
12/02/2020	1.31	0.97	1.11	124.32	7.70	100
14/02/2020	0.33	−0.15	0.08	30.78	51.46	127
18/02/2020	0.29	0.04	0.17	80.10	1.20	79
20/02/2020	1.19	0.32	0.78	84.94	34.81	74
22/02/2020	−0.07	−0.54	−0.25	75.87	21.35	83
24/02/2020	0.27	−0.67	−0.19	5.60	55.39	155
28/02/2020	0.26	−0.29	−0.04	57.34	27.97	89
02/03/2020	0.44	0.29	0.36	5.90	24.27	75
05/03/2020	0.28	0.06	0.15	51.29	51.68	128
12/03/2020	0.46	−0.17	0.14	5.63	34.76	55
15/03/2020	0.41	−0.02	0.22	50.23	54.71	163
18/03/2020	−0.17	−0.42	−0.26	30.98	10.92	44
20/03/2020	0.97	0.69	0.85	111.26	12.39	93
22/03/2020	−0.02	−0.18	−0.09	4.85	33.12	87
25/03/2020	0.85	0.37	0.65	51.54	36.76	89
26/03/2020	0.69	0.63	0.65	56.72	27.58	66

measured at the buoy (25th percentile = 0.65 m, 75th percentile = 0.69 m). In this latter case the two trajectories (1 - Jason-3 descending and 2 - Sentinel-3A descending) present a similar profile with the overall SWH ranging between 0.55 m and 2.49 m. In addition, both the altimeters recorded values close to 0.55 m in the lower part of the study area where the buoy was located.

To generalise the above results, the interpolate-buoy difference computed for the entire time period was plotted together with the statistics of the SWH values recorded from satellite altimeters, and wind speed spatial standard deviation for the area 1. In doing so, we reasonably assumed that the wind speed can be used as proxy for the SWH, i.e. high wind speed generates high SWH and vice versa. Standard deviation of wind speed was computed from the distribution of the wind field extracted from the second level products presented in the method. Fig. 14 a,b show that there is no relationship between the interpolation-buoy difference and the distribution of along-track values from the altimeter from the same date. On the other hand, good estimates of the SWH were observed when the wind field was characterised by minor spatial changes, i.e. low standard deviation values (Fig. 14c). Conversely, high interpolation-buoy differences happened closed to dates characterised by high spatial variability, i.e. high variance. Unfortunately, the gap between dates for which wind speed data and altimeters data were available does not allow a more precise comparison.

6. Discussion

Results have shown how the use of second level products from SAR satellites and data from altimeters can be used to easily quantify spatial uncertainty in wind power and SWH predictions. High resolution information, e.g. 10 m, can be extracted for wind speed and SWH, respectively from wind field maps retrieved from SAR imagery and sea surface maps obtained by interpolating along-track satellite measurements. In particular, the method proposed to generate 2D maps of SWH for the study area has showed that high accuracy results can be obtained also with few trajectories, i.e. low number of along-track measurements. Such wind speed and SWH products will generate information that can contribute to reduce costs during design and operation stages of an offshore wind farm life time.

6.1. The use of wind speed products to inform the site choice and design of offshore wind farms

Quantification of temporal and spatial uncertainty in local wind speed values will increase cost efficiency in offshore wind farm management. Statistical forecasts generated as ensembles of several results from deterministic NWP have been found to be a valid method to asses temporal uncertainty in weather forecasts and on-site measurements (Sweeney et al., 2020). This approach has been shown to be relevant also for short-term forecasting, which provides the measurements used to predict wind production or design maintenance operations (Gilbert et al., 2020). have used values on wind energy production extracted from existing turbines to compute the covariance between coupled of wind turbines within a wind farm. The covariance was used to modify a Gaussian distribution such that to have a probability distribution accounting for spatial structures existing between turbines. The probabilistic values were used to modify production values estimated from deterministic weather forecasts. Results have revealed how such method can reduce differences between forecast prediction and simulations by up to 5% compare to deterministic ones (Gilbert et al., 2020). Other methods such as Artificial Neural Networks (ANN), used trained artificial networks to link SAR imagery to sea state characteristics (Torres et al., 2012; Tapoglou and Dorrell, 2020).

We estimate the spatial variations in power compared to assuming a single value of wind to characterize the wind field within the portion of sea occupied by an offshore wind farm as typically done when adopting the NWP as outlined above. To do this we introduced few simplifying assumptions, i.e. 10 m wind speed up to hub height for an assumed turbine type such that to assign the parameters required for power estimation according to equation (2). Indeed, rather than provide precise values for wind power, the aim was to provide evidences of the potential of the use of wind speed satellite products to generate *a priori* values that can support decision making during site selection and design stages.

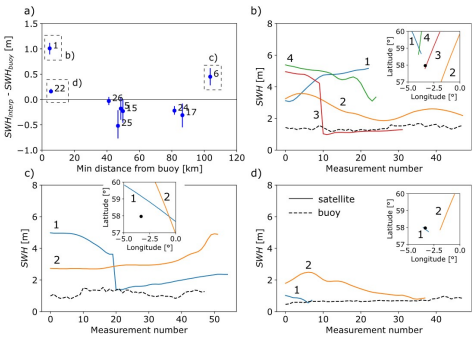

Fig. 13. Panel a shows the relationship between the interpolate-buoy difference and the minimum distance of the satellite trajectories from the buoy. Labels indicate the date, circles and vertical lines represent, respectively, the interpolated-buoy difference obtained by using the mean daily value recorded at the buoy, the 25th and 75th percentile of the daily distribution of the measurements at the buoy. Panels b, c, d show the SWH profile extracted from the buoy measurements (dashed black line) and along-track measurements for the different satellites used for the interpolation (continuous coloured lines), respectively for the dates 6, 22, and 24 January 2020. Close ups represent the spatial distribution of satellite trajectories and buoy. Black arrows indicate the direction the measurements for SWH were taken, i.e satellite ascending/descending trajectory.

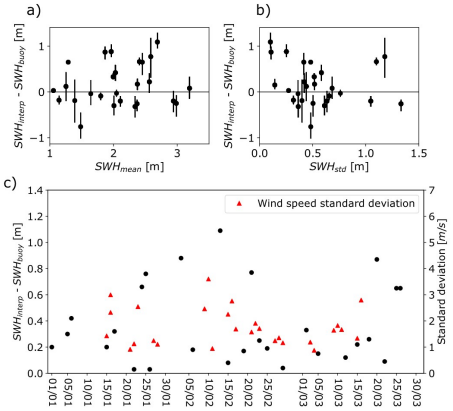

Fig. 14. Interpolate-buoy difference computed as the interpolated value extracted at the buoy and the mean (circle), the 25th percentile (vertical line lower extreme), and the 75th percentile (vertical line upper extreme) of the daily distribution of the measurements collected at the buoy plotted against the a) mean of SWH, b) standard deviation of SWH, and c) standard deviation of wind speed (red triangles).

The future development of this work will require a detail analysis of the uncertainties associated to the choice of the power coefficient C_p in equation (2) and adjustments in wind speed which will be conducted by comparing results with real energy production values. It is here anticipated, however, that exact values are difficult to obtain since they represent sensitive industrial information.

6.2. The use of SWH products to support decisions during construction and operation stages of offshore wind farms life time

Comparison of interpolating data with local measurements recorded at a marine buoy has revealed a strong influence of interpolating mesh resolution on data results, with mean error ranging from 3 m to 0.4 m by varying cells dimensions and interpolating method used. In particular, it was found that a cell ratio of 1.5 and 1.8 provided the minimum observed error for nearest and cubic method, respectively (Fig. 10). However, cubic method generates higher spatial resolute maps and for management purposes it may be worth loosing 0.1 m precision on the average SWH and increase information on its spatial distribution (see Fig. 8).

Quality of the results from interpolations seems to be more related to the disturbances on water surface induced by wind than spatial distribution of satellite trajectories or overall distance of the along-track measurements from the buoy (see comparisons on Fig. 12). Results are in agreement with observations on spatial variability of concurrent measurements between buoys (Barrett et al., 2009). In their analysis (Barrett et al., 2009), did not find any relationship between average SWH difference and buoy spatial distance, although they highlight an increasing spatial variability in measurements when distance increases. The present analysis further extends such observations by adding temporal uncertainty to spatial uncertainty, by interpolating results from non-concurrent measurements and comparing the value extracted at the buoy position with the mean, 25th percentile, and 75th percentile of the distribution of daily SWH measurements.

When the sea surface is homogeneous, results have shown that the interpolation provides more reliable results for SWH than in the case where the sea surface shows high spatial changes within the study area. Because different trajectories are related to different time during the time interval considered, it is reasonable to assume that this is due to a storm that has heavily modified the sea surface. Indeed, in absence of storms the sea surface may appear quite homogeneous for a long range distance, with waves characterized by long wave lengths and low energy propagating through the sea. On the other hand, close to a storm event, sea level can change rapidly in time according to the storm trajectory, inducing high spatial changes within 24-h time window. Under this considerations, it is reasonable to associate both spatial changes and error in the interpolated values to the spatial variability, i.e. standard deviation, of wind speed. Fig. 14 shows the comparison between wind spatial speed standard deviation and the interpolate-buoy difference. High values of difference can be associated to high values of standard deviation and vice versa. However, the limited amount of dates available, and the difficulty to collect data from the same dates limited the quality of the analysis and prevent a definite trend to be recognized. Collection of more data should be sought in the future to further investigate the inferred relationship.

7. Conclusions

We propose an innovative use of second level satellite products to quantify the uncertainty associated to wind speed and wave height measurements which adds costs during the life cycle of offshore wind farms. The method was intentionally kept at the minimum level of complexity such that it can be easily performed, and only requires open source satellite data.

We showed how detailed maps on wind field freely available can be used to quantify the error in wind power production for each section of the offshore plant domain by assigning a reference value, e.g. wind product estimated by using a local measurement or from the value of wind speed available from large weather forecast modelling.

A new method was proposed to spatially distribute along-track measurements from satellite altimeters over the domain of interest. The method consists in collecting all the trajectories available within a 24-h time window and interpolate all the measurements over a regular grid. A sensitivity analysis conducted on grid cells resolution have identify the existing of a specific ratio between cells in the y and x direction that minimize the error in interpolated values.

Results have revealed that the overall accuracy of the SWH values generated is not affected by spatial distribution of satellite trajectories within the study area, nor the distance of the along-track measurements from a specific point on the sea surface. There seems to exist a relationship with spatial changes in wind speed, i.e standard deviation, which appears reasonable to associate to sea storms. However, due to the limited dates available and the lack of concurrent measurements for wind speed and SWH such influence could only be inferred from results interpretation.

We argued that spatial distribution resulting from the proposed method can be combined with NWP and on-site measurements to propagate spatial uncertainty. Particularly, wind speed products will increase the efficiency in selecting the best site and design the layout of a wind farm. While, data on SWH will be used directly or to inform costs and stochastic modelling, to increase reliability in the choice of windows available to dispatch vessels. This will ultimately reduce costs during construction and operation phases of offshore wind farms life cycles.

Finally, the rapid increase in the frequency with which satellite data are available will increase the accuracy in estimating spatial changes in sea surface conditions within offshore wind farms (Medina-Lopez et al., 2020), further improving the efficiency of the method proposed in reducing lifetime costs for offshore wind farms.

Declaration of competing interest

The authors declare that they have no known competing financial interests or personal relationships that could have appeared to influence the work reported in this paper.

Acknowledgements

The authors thank the three anonymous reviewers whose comments helped to improve the manuscript. The work presented in this paper has been supported by SCORE grant funded by Supergen ORE-Hub (EPSRC).

References

Ahsbahs, T., Badger, M., Karagali, I., Larsén, X.G., 2017. Validation of sentinel-1a sar coastal wind speeds against scanning lidar. Rem. Sens. 9, 552.

Badger, M., Badger, J., Nielsen, M., Hasager, C.B., Peña, A., 2010. Wind class sampling of satellite sar imagery for offshore wind resource mapping. J. Appl. Meteorol. Climatol. 49, 2474–2491.

Barrett, S., Ashton, I., Lewis, T., Smith, G., 2009. Spatial & spectral variation of seaways. In: Proceedings of the 8th European Wave and Tidal Energy Conference.

Beatrice offshore wind farm (accessed September 9, 2020). URL. https://www.beatricewind.com.

Browell, J., Dinwoodie, I., McMillan, D., 2016. Forecasting for Day-Ahead Offshore Maintenance Scheduling under Uncertainty.

Brown, A.G., et al., 2018. Metocean Procedures Guide for Offshore Renewables. Modern Transactions of the IMarEST.

Carroll, J., McDonald, A., McMillan, D., 2016. Failure rate, repair time and unscheduled o&m cost analysis of offshore wind turbines. Wind Energy 19, 1107–1119.

Centre for Environment, 2020. Fisheries and Aquaculture Science (CEFAS). Available online. CEFASâ€"WaveNet (accessed June 26, 2020). URL. www.cefas.co.uk/cefas-data-hub/wavenet/.

Charnock, H., 1955. Wind stress on a water surface. Q. J. R. Meteorol. Soc. 81, 639–640.

Copernicus Marine Service, 2020a. ATLANTIC - EUROPEAN NORTH WEST SHELF - OCEAN WAVE ANALYSIS AND FORECAST. Available online. https://resources.marine.copernicus.eu. (Accessed 30 June 2020).

Copernicus Marine Service, 2020b. global ocean L3 significant wave height from NRT satellite measurements. Available online. https://resources.marine.copernicus.eu. (Accessed 1 July 2020).

European Centre for Medium-range weather forecasts (ECMWF). Public Datasets. Available online. https://www.ecmwf.int/en/forecasts/datasets-. (Accessed 26 June 2020).

European Space Agency (Esa), 2020. Sentinel-1 mission (accessed June 30, 2020). URL. https://sentinel.esa.int/web/sentinel/missions/sentinel-1.

Flores-Anderson, A.I., Herndon, K.E., Thapa, R.B., Cherrington, E., 2019. The Sar Handbook: Comprehensive Methodologies for Forest Monitoring and Biomass Estimation.

Gilbert, C., Browell, J., McMillan, D., 2020. Leveraging turbine-level data for improved probabilistic wind power forecasting. IEEE Trans. Sustain. Energy 11 (3), 1152–1160.

Hersbach, H., de Rosnay, P., Bell, B., Schepers, D., Simmons, A., Soci, C., Abdalla, S., Alonso-Balmaseda, M., Balsamo, G., Bechtold, P., et al., 2018. Operational Global Reanalysis: Progress, Future Directions and Synergies with Nwp, Era Report Series 27. ecmwf, Reading, UK.
Holthuijsen, L.H., 2010. Waves in Oceanic and Coastal Waters. Cambridge university press.
Hou, P., Zhu, J., Ma, K., Yang, G., Hu, W., Chen, Z., 2019. A review of offshore wind farm layout optimization and electrical system design methods. J. Mod. Power Syst. Clean Energy 7, 975–986.
Lacal-Arántegui, R., Yusta, J.M., Domínguez-Navarro, J.A., 2018. Offshore wind installation: analysing the evidence behind improvements in installation time. Renew. Sustain. Energy Rev. 92, 133–145.
Leithead, W., 2007. Wind energy. Phil. Trans. Math. Phys. Eng. Sci. 365, 957–970.
Maples, B., Saur, G., Hand, M., Van De Pietermen, R., Obdam, T., 2013. Installation, Operation, and Maintenance Strategies to Reduce the Cost of Offshore Wind Energy. Technical Report. National Renewable Energy Lab.(NREL), Golden, CO (United States).
Medina-Lopez, E., McMillan, D., Lazic, J., Hart, E., Zen, S., Angeloudis, A., Bannon, E., Browell, J., Dorling, S., Dorrell, R., Forster, R., Old, C., Payne, G., Porter, G., Rabaneda, A., Sellar, B., Tapoglou, E., Trifonova, N., Woodhouse, I., Zampollo, A., 2020. Satellite Data for the Offshore Renewable Energy Sector: Synergies and Innovation Opportunities. Renewable & Sustainable Energy Reviews. Under review).
Monaldo, F., Jackson, C., Li, X., Pichel, W.G., 2016. Preliminary evaluation of sentinel-1a wind speed retrievals. IEEE J. Select. Top. Appl. Earth Observ. Remote Sens. 9, 2638–2642.
Rana, F.M., Adamo, M., Lucas, R., Blonda, P., 2019. Sea surface wind retrieval in coastal areas by means of sentinel-1 and numerical weather prediction model data. Remote Sens. Environ. 225, 379–391.
Schneiderhan, T., Lehner, S., Schulz-Stellenfleth, J., Horstmann, J., 2005. Comparison of offshore wind park sites using sar wind measurement techniques. Meteorol. Appl. 12, 101–110.
Sempreviva, A.M., Barthelmie, R.J., Pryor, S., 2008. Review of methodologies for offshore wind resource assessment in european seas. Surv. Geophys. 29, 471–497.
Seyr, H., Muskulus, M., 2019. Decision support models for operations and maintenance for offshore wind farms: a review. Appl. Sci. 9, 278.
Sweeney, C., Bessa, R.J., Browell, J., Pinson, P., 2020. The future of forecasting for renewable energy. Wiley Interdisciplinary Rev.: Energy Environ. 9, e365.
Tapoglou, E., Forster, R.M., Dorrell, R.M., 2020. Satellite-based machine learning for sea-state prediction in an offshore windfarm. Remote Sens. Environ (under review).
Taylor, J.W., Jeon, J., 2018. Probabilistic forecasting of wave height for offshore wind turbine maintenance. Eur. J. Oper. Res. 267, 877–890.
Tennekes, H., 1973. The logarithmic wind profile. J. Atmos. Sci. 30, 234–238.
Torres, R., Snoeij, P., Geudtner, D., Bibby, D., Davidson, M., Attema, E., Potin, P., Rommen, B., Floury, N., Brown, M., et al., 2012. Gmes sentinel-1 mission. Remote Sens. Environ. 120, 9–24.
Ulaby, F.T., Moore, R.K., Fung, A.K., 1982. Microwave Remote Sensing Active and Passive-Volume II: Radar Remote Sensing and Surface Scattering and Enission Theory. Technical Report. Addison-Wesley Publishing CompanyAdvanced Book Program/World Science Division.
WaveNet CEFAS, 2020. http://wavenet.cefas.co.uk/Map (accessed September 9, 2020).
Satellite Winds, DTU Wind Energy, 2020. Department ofWind Energy (accessed September 2, 2020). https://satwinds.windenergy.dtu.dk/.
Yang, J., Zhang, J., 2019. Validation of sentinel-3a/3b satellite altimetry wave heights with buoy and jason-3 data. Sensors 19, 2914.
Zecchetto, S., 2018. Wind direction extraction from sar in coastal areas. Rem. Sens. 10, 261.